Nano Research 2015, 8(11): 3715–3724
DOI 10.1007/s12274-015-0871-2
Research Article
ISSN 1998-0124
CN 11-5974/O4

Silver-coated elevated bowtie nanoantenna arrays: Improving the near-field enhancement of gap cavities for highly active surface-enhanced Raman scattering

Lei Feng[§], Renping Ma[§], Yandong Wang, Daren Xu, Dongyang Xiao, Lingxiao Liu, and Nan Lu (✉)

State Key Laboratory of Supramolecular Structure and Materials, Jilin University, Changchun 130012, China
[§] *These authors contributed equally to this work.*

Received: 16 March 2015
Revised: 25 July 2015
Accepted: 30 July 2015

KEYWORDS
surface-enhanced Raman scattering (SERS), surface plasmon resonance, bowtie nanoantenna, nanosphere lithography, gap cavity

ABSTRACT

Improving hot-spot intensity is a key issue in surface-enhanced Raman scattering (SERS). The bowtie nanoantenna (BNA) is an effective device used to concentrate light energy into a nanoscale volume and produce strong hot spots. Nanosphere lithography (NSL) is a large-area and low-cost technique to produce BNA arrays; however, the SERS activity of NSL-fabricated BNAs is limited. In this paper, we present a simple method to improve the SERS activity of conventional NSL-fabricated BNAs by modifying their geometry. The new configuration is termed "silver-coated elevated bowtie nanoantenna" (SCEBNA). SCEBNAs perform intensive near-field enhancement in the gap cavities owing to the integrated contribution of the "lightning rod" effect, resonance coupling, and the formation of the plasmonic Fabry–Pérot cavity. Experimental measurements and finite-difference time-domain simulations revealed that the hot-spot intensity and the substrate enhancement factor can be optimized by adjusting the silver thickness. The optimal sample has the capability of trace-amount detection with fine reproducibility.

1 Introduction

Benefiting from recent developments in nanofabrication and the ongoing studies on plasmonics, surface-enhanced Raman scattering (SERS) spectroscopy is a powerful technique in chemical and biological sensing owing to its ultrasensitivity and the capability to provide molecular fingerprints [1–6]. One key issue concerning the practical application of SERS is the fabrication of highly active and reproducible substrates [7, 8]. According to the electromagnetic mechanism, the substrates use sites with small volumes and extremely concentrated electromagnetic fields to excite the remarkable Raman radiation of the adsorbed molecules; these sites are termed "hot spots" [9–11]. It has been experimentally demonstrated that only 1% of molecules at the hot spots with an enhancement factor (EF) larger than 10^7 can contribute almost 70% to the overall SERS

Address correspondence to luenan@jlu.edu.cn

signal on a silver-film-over-nanosphere substrate [12]. This result illuminates the significance of increasing the hot-spot intensity for improving the average EF of the substrate [13].

A noble-metal bowtie nanoantenna (BNA) can serve as a device that confines and localizes optical radiation into a nanoscale volume, achieving excellent field concentration [14, 15]. It has been applied in not only surface-enhanced spectroscopies [16–19], but also nonlinear optics [20–22], optical tweezers [23], photocatalysis [24], and biosensing [25]. All these applications depend on the hot spots near the gap between two adjacent triangle tips where the "lightning rod" effect and the resonance coupling occur [11, 26, 27]. The "lightning rod" effect is a frequency-independent phenomenon, in which the local charge is fiercely compressed at the triangle tips under excitation by electromagnetic waves polarized along the tip axis; thus, the local fields in the vicinity of the tips are enhanced [28, 29]. Resonance coupling is the interaction of the frequency-dependent plasmon resonances of two individual nanotriangles. According to plasmon hybridization theory, the large field enhancement in the gap results from the admixture of the higher-order multipolar resonances of each individual nanotriangle into the bonding dipolar dimer modes of the BNA [30]. By decreasing the separation of the two nanotriangles, more higher-order multipolar resonances can contribute to this admixture. Therefore, the hot-spot intensity can be enhanced by minimizing the radius of curvature of the tips and the gap size. Considerable technical effort has been devoted to the fabrication of the subtle features, whereas high-precision fabrication techniques are difficult and time-consuming [18–20, 26, 31–34]. Moreover, shrinking the gap volume means decreasing the probability of Raman molecules being assembled in the hot-spot region, which degrades the performances of the SERS substrates, especially for low-concentration and reproducible measurements [5, 8, 35]. The transformation of the BNA geometry is another solution to improve hot-spot intensity. Schuck et al. reported an evolved configuration termed "asymmetric bowtie nanocolorsorters", where two BNAs are oriented in a "cross" configuration. The additional BNA induces a new coupling regime causing a further enhancement of the gap fields by adjusting the symmetry of the system [36]. Gu's group fabricated an elevated BNA, which is a BNA supported by two underlying silicon pillars [17]. This configuration can reduce the substrate effect by exposing a larger volume with enhanced fields to excite the Raman scattering of molecules [37]. Besides, the silicon pillars maintain the localized surface plasmons (LSPs) of the BNA near the anti-node of the standing wave in the Fabry–Pérot cavity [17, 38–40]. This generates more efficient excitation of the bowtie LSP and, thus, stronger hot spots.

BNAs, either with subtle features or evolved configurations, are usually fabricated using scanning beam lithography (SBL) [41]. SBL can be used to precisely produce nano-bowties with a high resolution and an arbitrary variation of the geometrical parameters. However, the high cost and low throughput of SBL limit its extensive use as a serial technique. Nanosphere lithography (NSL) is another technique that can be used to fabricate BNA arrays in a large area with high throughput and low cost, but the geometrical parameters are limited. For example, the gap size and the triangle size of the bowtie restrict each other. As mentioned above, to achieve efficient resonance coupling, the gap size must be small enough [30], which requires a small diameter of the closely packed nanospheres. However, for the coupling of sufficient higher-order multipolar resonances of each nanotriangle with the bonding dipolar mode, the triangle size cannot be too small [30], which demands relatively large nanospheres. This intrinsic conflict limits the EF of NSL-fabricated BNAs to below the order of ~10^8, typically 10^7 [42].

Therefore, the parallel fabrication of BNA-based structures that can achieve improved field enhancement with no need for subtle features, e.g., sub-10-nm gaps [17], is significant for the practical applications of highly sensitive SERS. Herein, we demonstrate a method using NSL to produce an evolved BNA configuration, the silver-coated elevated bowtie nanoantenna (SCEBNA). The SERS activity of SCEBNAs is superior to that of conventional NSL-fabricated BNAs. Intensive hot spots, located at gaps with a few tens of nanometers, can be generated owing to the integrated contributions of the "lightning rod" effect, resonance coupling, and the formation of plasmonic

Fabry–Pérot cavities. We investigated the dependence of the hot-spot intensity on the thickness of the silver coating. The optimized substrate was highly SERS active, showing a capability of trace-amount detection with fine reproducibility.

2 Results and discussion

Figure 1 shows the fabrication process of the SCEBNA. We first prepared a self-assembled monolayer (SAM) of close-packed polystyrene (PS) nanospheres on the Si substrate, as described elsewhere [43]. The diameter of the PS spheres was 360 nm, which is sufficiently small to produce high-density BNAs. The SAM of the PS spheres was etched by oxygen plasma to reduce the separation between adjacent triangular voids. 30-nm-thick Au was deposited on the substrate with the etched SAM of the PS spheres as a template and then the PS spheres were dissolved in tetrahydrofuran. The remaining Au nanotriangles served as masks in the subsequent reactive ion etching to produce the Si pillars. The Si pillars were 80 nm in height and elevated the Au bowties, as shown in Fig. 2(a). We evaporated silver coatings of different thicknesses

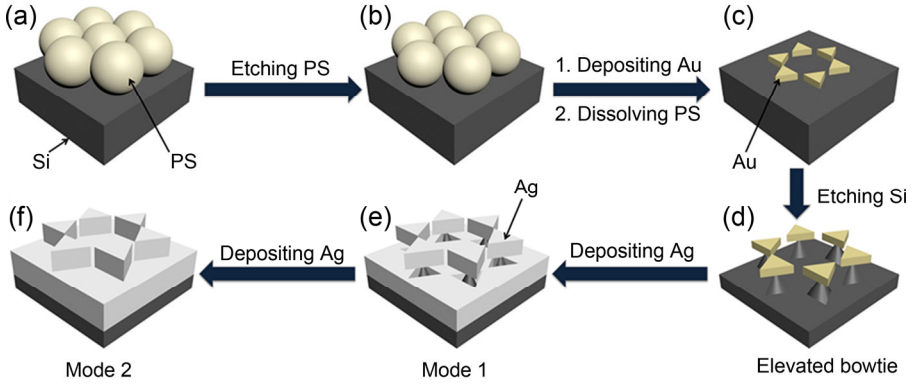

Figure 1 Schematic of the fabrication process of the SCEBNAs. (a) The SAM of PS nanospheres is prepared on the Si substrate. (b) The PS spheres are etched by O_2 plasma to reduce their diameter. (c) The PS spheres are coated with a layer of Au and then dissolved in tetrahydrofuran to remain the Au bowtie array. (d) Si is etched by reactive ions to form the elevated bowties. (e) and (f) Silver coatings with different thicknesses are then deposited on the elevated bowties, forming two modes of SCEBNA arrays.

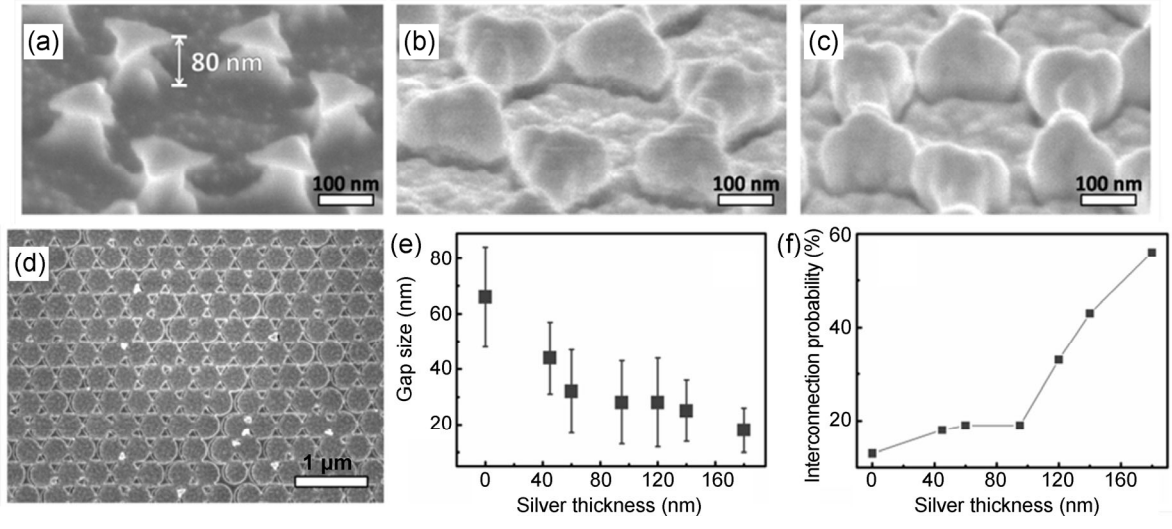

Figure 2 (a)–(c) SEM images of SCEBNAs with different thicknesses of silver: (a) 0 nm, (b) 60 nm, and (c) 95 nm. The scale bars represent 100 nm. (d) SEM images of the SCEBNA array in a ~20 μm^2 area. The scale bar represents 1 μm. (e) The average gap size of the SCEBNA arrays with different silver thickness. The error bars indicate the standard deviation. (f) The linkage probability at the positions where gaps are expected to be present.

onto the substrates, so that both the Au bowties and the unmasked regions were covered. Herein, the silver film on the unmasked regions is termed "baseplate." When the thickness of the silver coating was smaller than the height of the Si pillars, e.g., 60 nm, a vertical separation existed between the baseplate and the upper bowties, as shown in Fig. 2(b). When the silver thickness exceeded the height of the Si pillars, e.g., 95 nm, this separation disappeared, as shown in Fig. 2(c). These two configurations are termed mode 1 and mode 2, respectively. Scanning electron microscope (SEM) images of samples with different silver thickness are shown in Fig. S1 in the Electronic Supplementary Material (ESM). Moreover, by measuring the gaps within a large area, as illustrated in Fig. 2(d), we have plotted the average gap size and the linkage probability along with the variation of the silver thickness, as shown in Figs. 2(e) and 2(f), respectively. Every data point was obtained by statistical analysis of 100 random gaps. By increasing the silver thickness, the gap size decreased gradually and more linkages appeared at the positions where gaps were expected to be present. This is due to the isotropy of the silver evaporation process.

To investigate the SERS activity of the SCEBNA, we measured the Raman spectra after the introduction of 4-mercaptopyridine (4-MPy) as probe molecules (see Fig. 3(a)). 4-MPy molecules can disperse across the surface of the SCEBNAs free from the confinement of size selectivity because the coverage is only ~2.77 nm^2 per molecule [44]. In the Raman tests, as described in the Method Section, the elevated bowtie array is not SERS-active. Only after the deposition of silver, the Raman spectra of 4-MPy can be identified. All the profiles of the Raman spectra were analogous to previously reported ones, and it has been confirmed that every 4-MPy molecule is adsorbed on the silver surface monodispersedly and perpendicularly via a S-Ag bond [45]. The most intense peak, which can be used to characterize the SCEBNA arrays' SERS sensitivities, was located at 1,091 cm^{-1} and generated by the vibration coupling between the substitute and pyridine ring of 4-Mpy [45]. Comparing all the peaks at 1,091 cm^{-1} with the aforementioned samples used as substrates (see Fig. 3(b)), it can be seen that the peak value first increases and then decreases with

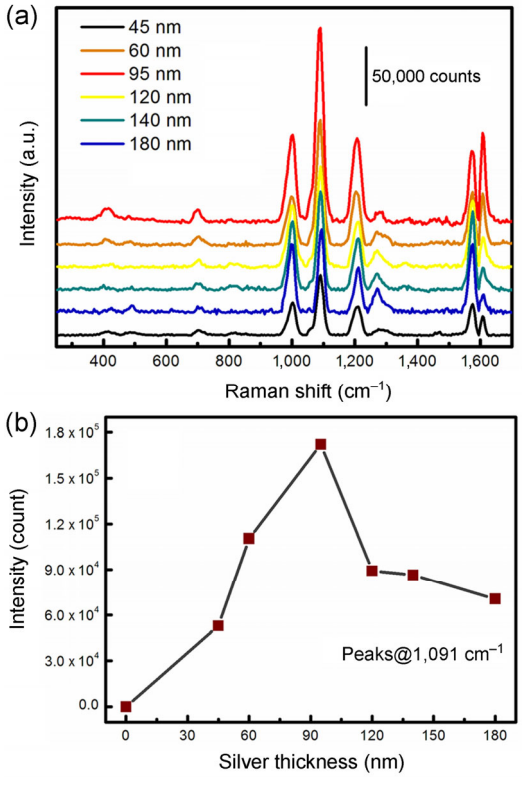

Figure 3 (a) SERS spectra of 10^{-5} M 4-MPy adsorbed on SCEBNAs with different silver coating thicknesses. The wavelength of the laser was 532 nm and the integration time was 2 s. The scale bar represents 50,000 counts. (b) Correlation between the SERS intensity at 1,091 cm^{-1} and the thickness of silver.

increasing silver thickness. The highest enhancement is observed for the 95-nm sample, whose maximum EF is 9.8×10^9. Details about the EF calculation are provided in Section S2 of the ESM.

The plasmonic resonance features of the SCEBNAs were studied using the finite-difference time-domain (FDTD) simulations. Figures 4(a)–4(f) are the contour plots of the electric field intensity distribution near the elevated bowties with 0-, 60-, and 95-nm-thick silver coatings. The incident plane wave was incident along the negative z-direction and polarized parallel to the x-axis with a wavelength of 532 nm. Here, the gap size in every sample equals to the average one, as shown in Fig. 2(e). More details about the modeling are illustrated in Fig. S3 in the ESM, and the field distribution plots with other silver thicknesses are shown in Fig. S4 in the ESM. In the absence of silver coating, as shown in Figs. 4(a) and 4(b), the electric field at the gap was weak because of the large separation between the adjacent gold triangles (~66 nm); as a result,

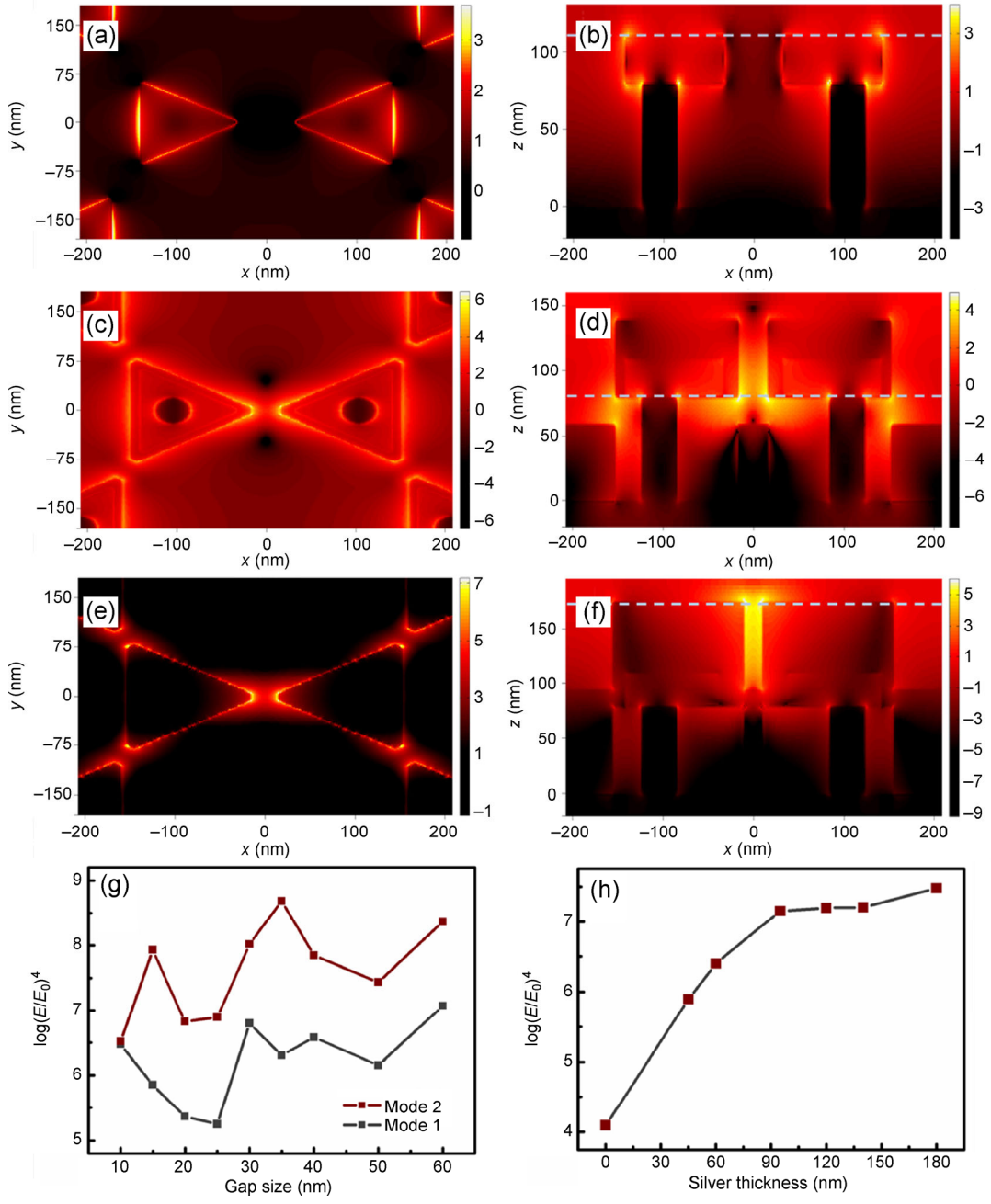

Figure 4 (a), (c), and (e) Top-view and (b), (d), and (f) side-view contour plots of the electric field intensity distribution near the SCEBNAs for various thicknesses of silver: (a) and (b) 0 nm, (c) and (d) 60 nm, and (e) and (f) 95 nm. The altitude of each top-view plot is marked with the dash line in the corresponding side-view plot. The color bar is in the scale of $\log(E/E_0)^4$. (g) Correlation between the maximum EF of the SCEBNAs and the gap size. Modes 1 and 2 indicate SCEBNA arrays with 60- and 95-nm-thick silver coatings. (h) The simulated EF of the SCEBNAs with different silver thickness. Every data point was calculated with a gap size equal to the corresponding average value.

no efficient near-field coupling could be generated [17].

Clearly, the silver coating contributed to the concentration of the light fields. After introducing a 60-nm-thick silver coating (mode 1), the gap size decreased to ~32 nm whereas the triangle size increased. In the horizontal direction, as shown in Fig. 4(c), the local fields at the tip-to-tip positions were further intensified owing to the increasing LSP momentum of the individual triangles and the improved coupling efficiency between them. The most intense sites were

located within gaps perpendicular to the *x*-axis because both the "lightning rod" effect and resonance coupling are polarization-dependent [28, 46]. In the vertical direction, as shown in Fig. 4(d), the fields were enhanced where the lower baseplate was close to the gap and the edge of the upper bowtie. This is because of the near-field coupling between the bowties and the baseplate [38, 47–49]. In mode 1, hot spots were distributed in a variety of positions and the strongest one was located at the bottom side of the gap, perpendicular to the polarization direction of the incident light.

When the silver thickness was further increased to 95 nm (mode 2), the baseplate was in contact with the bowties and the vertical coupling disappeared. In this configuration, the gap size was lowered to ~28 nm and the triangle size kept increasing. Both the "lightning rod" effect and resonance coupling were further reinforced. The horizontal location of the hot spots was similar to that of mode 1, as shown in Fig. 4(e). However, in the vertical direction, the hot spots shifted to the gap top, as shown in Fig. 4(f). Mode 2 was a plasmonic Fabry–Pérot cavity mode [39, 50, 51]. Along the sidewalls of the gap, transverse surface plasmons were excited by the incident laser and interfered with the ones reflected by the baseplate. The sidewall length was approximately a quarter of the wavelength of the standing wave, whose node and anti-node were located at the baseplate and the gap top, respectively. Because of the disappearance of the vertical coupling, no other parts of the structure except the gaps could generate hot spots.

The above analysis is based on the assumption that the gap size equals the average value. However, in the real samples, the gap size varied owing to fabrication deviations. To comprehensively discuss the hot-spot intensity variation during mode transition, we calculated the maximum EF of modes 1 and 2 with gap sizes ranging from 10 to 60 nm, as shown in Fig. 4(g). When the same gap size was considered for the two modes, the maximum EFs in mode 2 were larger than those in mode 1. This may be the consequence of the fact that the field-enhanced volume in mode 2 is smaller than that in mode 1. The electromagnetic energy can be better confined and concentrated in mode 2. Another resonance feature is the non-monotonic correlation between the maximum EF and the gap size in both modes. The mechanism is comprehensive. When the gap size decreases, the resonance coupling between adjacent triangles is enhanced [17]. On the other hand, the optical reflection at the 532 nm wavelength decreases with increasing the gap size, as shown in Fig. S5 in the ESM. This is due to the reduction of the effective refractive index of the structure, which induces better impedance matching between the air and the substrate [52]. More free-space light can couple into surface plasmons to generate stronger hot spots [53]. Meanwhile, the gap size increase reduces the wavelength of the standing wave in the cavity under the same excitation [50]. We speculate that the altitude difference between the anti-node of the standing wave and the top side of the gap is another factor that affects the EF. Nonetheless, the overall factors indicate that a dramatic field enhancement can be achieved even with a large gap size. In our simulation, the maximum EF was achieved with a 35-nm gap in mode 2.

We collected the maximum EFs of all the samples with different silver thicknesses and plotted them in Fig. 4(h), which demonstrates the dependence of the field enhancement on the silver thickness. When the thickness is 0, the EF is the lowest because of the inefficient near-field coupling. When the thickness is 45 or 60 nm, the EF is much higher owing to the strong coupling regime. The 60-nm sample has a stronger vertical coupling between the baseplate and the bowties than the 45-nm sample so that the EF increases with the thickness. When the thickness is further increased, the system transforms into mode 2. The EF increase during the mode transition is attributed to the improvement of the integrated contribution of the "lightning rod" effect, resonance coupling, and the reduced hot-spot volume after the formation of the plasmonic Fabry–Pérot cavity. The four samples with 95-, 120-, 140-, and 180-nm-thick silver coatings have the same length of bowtie sidewall, but the gap size decreases gradually. A smaller gap generates better coupling between adjacent triangles so that the EF increases gradually. However, in the real fabrication process, increasing the thickness means that more triangles interconnect laterally owing to the isotropy of the silver evaporation process, as illustrated in Fig. 2(f). This results in the decrease of the hot-spot density and

the experimental EF. Considering these results, the variation of the SERS activity, as shown in Fig. 3(b), can be qualitatively interpreted.

As a result of the improved hot-spot intensity, the optimized SCEBNA array has the capability to detect trace-amount analytes. We measured the Raman spectra of 4-MPy molecules adsorbed on the 95-nm sample with concentrations ranging from 1.0×10^{-5} to 1.0×10^{-13} M under a 16-mW laser excitation with 2 s integrating time. As shown in Fig. 5(a), the SERS intensity decreases when reducing the concentration of 4-MPy, but the 1,003, 1,091, and 1,576 cm^{-1} peaks can be identified even with a 4-MPy concentration lower than 1.0×10^{-12} M. The detection limit may be further lowered by other means, such as increasing the integration time. We measured the peak intensities (I) at 1,003 cm^{-1} with different 4-MPy concentrations (C) and plotted them in Fig. 5(b). The linear fit was determined as $\log I = 0.1102 \times \log C + 5.3493$, and the multiple correlation coefficient was 0.95889. This shows the potential of quantitative detection. Furthermore, reproducibility is another important criterion for evaluating the performance of a SERS substrate. We collected the SERS spectra from 11 different positions in an area of 5 mm^2 on the 95-nm sample, as shown in Fig. 5(c). From the statistical analysis of the peak intensity at 1,003, 1,091, 1,207, and 1,576 cm^{-1}, we calculated the corresponding relative standard deviations as 15.45%, 13.27%, 10.58%, and 11.65%, respectively. The reproducibility is fine because of the ordered arrangement of the structure. Although the SCEBNA array is not absolutely ordered in the long range owing to the defects introduced by the assembly process, its ordering is still good enough to obtain reproducible SERS responses under an incident laser spot with a 50-μm diameter. Reproducible detectability is essential for both the accuracy of our experiment and the potential for further practical applications.

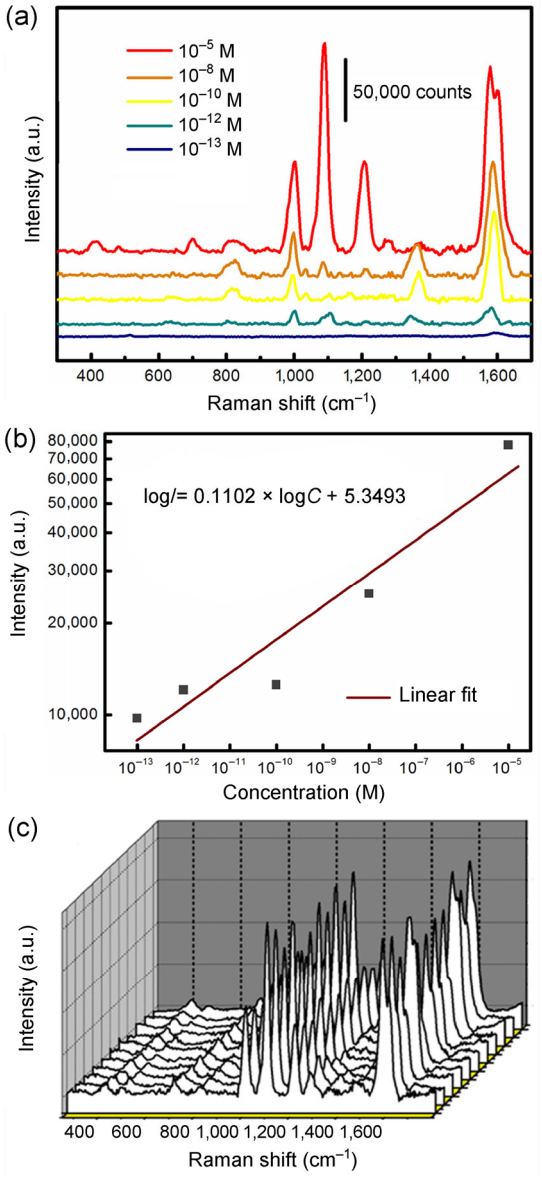

Figure 5 (a) SERS spectra of 4-MPy with different concentrations adsorbed on the SCEBNA arrays with 95-nm silver coating. The wavelength of the laser was 532 nm and the integration time was 2 s. The scale bar represents 50,000 counts. (b) The linear relationship between logarithmic intensities (1,003 cm^{-1}) and logarithmic concentrations. (c) SERS spectra of 4-MPy with a concentration of 10^{-5} M adsorbed at 11 random points. The integration time was 1 s.

3 Conclusions

In conclusion, we demonstrate a simple method to fabricate SCEBNA arrays serving as highly active substrates, which can perform reproducible trace-amount detection. The maximum EF is 9.8×10^9 owing to the integrated contribution of the "lightning rod" effect, resonance coupling, and the formation of the plasmonic Fabry–Pérot cavity. The near-field enhancement in the cavities can be tuned by adjusting the silver thickness. We believe that the substrate EF can be further optimized by precisely adjusting the thickness. The most intense hot spots can be generated even with no need for sub-10-nm gaps. This is

advantageous for SERS performance and facilitates fabrication. The developed methodology may also be suitable for other elevated structures.

4 Method Section

4.1 Fabrication of the SCEBNAs

The SAMs of the PS spheres were fabricated using a previously reported method [7, 54]. The Si wafers [n-type (100)] were purchased from GRINM Advanced Materials Co. Ltd., China, and the PS spheres were prepared as described elsewhere [43]. All the dry etching processes were performed using a Plasmalab Oxford 80 plus (ICP 65) system (Oxford Instrument Co., UK). During the oxygen plasma-etching step, the gas flow was 20-sccm O_2, the RF power was 30 W, and the chamber pressure was 10 mTorr. During the reactive ion etching step, the gas flow was a mixture of SF_6 (6 sccm), CHF_3 (45 sccm), and O_2 (8 sccm). The RF power was 100 W, and the chamber pressure was 8 mTorr. Metal thermal evaporation was performed in a homemade evaporation system, and the amount of evaporated metal was measured with a quartz crystal microbalance. The gold had 99.999% purity and was purchased from ZhongNuo Advanced Material (Beijing) Technology Co. Ltd., China. The silver had 99.999% purity and was purchased from Sinopharm Chemical Reagent Co. Ltd., China.

4.2 Sample characterization and SERS evaluation

The morphology features of the SCEBNAs were characterized using a JEOL JSM 6700F field emission SEM operated at 3.0 kV. The SERS activity of the SCEBNA arrays was evaluated by introducing 4-MPy (Sigma Aldrich) as probe molecules. A 10-μL droplet of aqueous solution (1.0×10^{-5} M) was first dropped on the substrate. After the evaporation of water in air, the 4-MPy molecules were absorbed on the silver surface forming a circular spot with a 3.5-mm diameter. We measured the SERS signal of the spot using an optical-fiber portable Raman spectrometer (B&W Tek Inc.) in the backscattering mode. The wavelength, power, and diameter of the incident laser beam were 532 nm, 16 mW, and 50 μm, respectively. The integration time was 2 s.

4.3 FDTD simulation

Lumerical FDTD Solutions software was used to simulate the field intensity and distribution near the SCEBNA structure. The dielectric coefficients of Au, Ag, and Si were obtained from Palik's handbook [55]. The mesh size was 1.5 nm in all three dimensions. More details about the modeling and calculation are provided in the ESM.

Acknowledgements

This work was supported by the National Natural Science Foundation of China (No. 21273092) and the National Basic Research Program of China (No. 2009CB939701).

Electronic Supplementary Material: Supplementary material (the SEM characterization, the calculation of the SERS enhancement factor, the modeling and results of the FDTD simulations) is available in the online version of this article at http://dx.doi.org/10.1007/s12274-015-0871-2.

References

[1] Natan, M. J. Concluding remarks: Surface enhanced Raman scattering. *Faraday Discuss.* **2006**, *132*, 321–328.

[2] Doering, W. E.; Piotti, M. E.; Natan, M. J.; Freeman, R. G. SERS as a foundation for nanoscale, optically detected biological labels. *Adv. Mater.* **2007**, *19*, 3100–3108.

[3] Ko, H.; Singamaneni, S.; Tsukruk, V. V. Nanostructured surfaces and assemblies as SERS media. *Small* **2008**, *4*, 1576–1599.

[4] Morton, S. M.; Silverstein, D. W.; Jensen, L. Theoretical studies of plasmonics using electronic structure methods. *Chem. Rev.* **2011**, *111*, 3962–3994.

[5] Kleinman, S. L.; Frontiera, R. R.; Henry, A. I.; Dieringer, J. A.; Van Duyne, R. P. Creating, characterizing, and controlling chemistry with SERS hot spots. *Phys. Chem. Chem. Phys.* **2013**, *15*, 21–36.

[6] Sun, Y. H.; Jiang, L.; Zhong, L. B.; Jiang, Y. Y.; Chen, X. D. Towards active plasmonic response devices. *Nano Res.* **2015**, *8*, 406–417.

[7] Wang, Y. D.; Lu, N.; Wang, W. T.; Liu, L. X.; Feng, L.; Zeng, Z. F.; Li, H. B.; Xu, W. Q.; Wu, Z. J.; Hu, W. et al. Highly effective and reproducible surface-enhanced Raman

scattering substrates based on Ag pyramidal arrays. *Nano Res.* **2013**, *6*, 159–166.

[8] Huang, J. A.; Zhao, Y. Q.; Zhang, X. J.; He, L. F.; Wong, T. L.; Chui, Y. S.; Zhang, W. J.; Lee, S. T. Ordered Ag/Si nanowires array: Wide-range surface-enhanced Raman spectroscopy for reproducible biomolecule detection. *Nano Lett.* **2013**, *13*, 5039–5045.

[9] Stockman, M. I. Electromagnetic theory of SERS. In *Surface-enhanced Raman Scattering: Physics and Applications*; Kneipp, K.; Moskovits, M.; Kneipp, H., Eds.; Springer-Verlag: Berlin, Heidelberg, 2006; pp 47–65.

[10] Banholzer, M. J.; Millstone, J. E.; Qin, L. D.; Mirkin, C. A. Rationally designed nanostructures for surface-enhanced Raman spectroscopy. *Chem. Soc. Rev.* **2008**, *37*, 885–897.

[11] Lal, S.; Grady, N. K.; Kundu, J.; Levin, C. S.; Lassiter, J. B.; Halas, N. J. Tailoring plasmonic substrates for surface enhanced spectroscopies. *Chem. Soc. Rev.* **2008**, *37*, 898–911.

[12] Fang, Y.; Seong, N. H.; Dlott, D. D. Measurement of the distribution of site enhancements in surface-enhanced Raman scattering. *Science* **2008**, *321*, 388–392.

[13] Le Ru, E. C.; Blackie, E.; Meyer, M.; Etchegoin, P. G. Surface enhanced Raman scattering enhancement factors: A comprehensive study. *J. Phys. Chem. C* **2007**, *111*, 13794–13803.

[14] Novotny, L.; van Hulst, N. Antennas for light. *Nat. Photonics* **2011**, *5*, 83–90.

[15] Liang, Z. Q.; Sun, J.; Jiang, Y. Y.; Jiang, L.; Chen, X. D. Plasmonic enhanced optoelectronic devices. *Plasmonics* **2014**, *9*, 859–866.

[16] Kinkhabwala, A.; Yu, Z. F.; Fan, S. H.; Avlasevich, Y.; Müllen, K.; Moerner, W. E. Large single-molecule fluorescence enhancements produced by a bowtie nanoantenna. *Nat. Photonics* **2009**, *3*, 654–657.

[17] Hatab, N. A.; Hsueh, C. H.; Gaddis, A. L.; Retterer, S. T.; Li, J. H.; Eres, G.; Zhang, Z. Y.; Gu, B. H. Free-standing optical gold bowtie nanoantenna with variable gap size for enhanced Raman spectroscopy. *Nano Lett.* **2010**, *10*, 4952–4955.

[18] Dai, Z. G.; Xiao, X. H.; Liao, L.; Zheng, J. F.; Mei, F.; Wu, W.; Ying, J. J.; Ren, F.; Jiang, C. Z. Large-area, well-ordered, uniform-sized bowtie nanoantenna arrays for surface enhanced Raman scattering substrate with ultra-sensitive detection. *Appl. Phys. Lett.* **2013**, *103*, 041903.

[19] Dodson, S.; Haggui, M.; Bachelot, R.; Plain, J.; Li, S. Z.; Xiong, Q. H. Optimizing electromagnetic hotspots in plasmonic bowtie nanoantennae. *J. Phys. Chem. Lett.* **2013**, *4*, 496–501.

[20] Hanke, T.; Krauss, G.; Träutlein, D.; Wild, B.; Bratschitsch, R.; Leitenstorfer, A. Efficient nonlinear light emission of single gold optical antennas driven by few-cycle near-infrared pulses. *Phys. Rev. Lett.* **2009**, *103*, 257404.

[21] Ko, K. D.; Kumar, A.; Fung, K. H.; Ambekar, R.; Liu, G. L.; Fang, N. X.; Toussaint, K. C. Nonlinear optical response from arrays of Au bowtie nanoantennas. *Nano Lett.* **2011**, *11*, 61–65.

[22] Suh, J. Y.; Huntington, M. D.; Kim, C. H.; Zhou, W.; Wasielewski, M. R.; Odom, T. W. Extraordinary nonlinear absorption in 3D bowtie nanoantennas. *Nano Lett.* **2012**, *12*, 269–274.

[23] Roxworthy, B. J.; Ko, K. D.; Kumar, A.; Fung, K. H.; Chow, E. K.; Liu, G. L.; Fang, N. X.; Toussaint, K. C., Jr. Application of plasmonic bowtie nanoantenna arrays for optical trapping, stacking, and sorting. *Nano Lett.* **2012**, *12*, 796–801.

[24] Salmistraro, M.; Schwartzberg, A.; Bao, W.; Depero, L. E.; Weber-Bargioni, A.; Cabrini, S.; Alessandri, I. Triggering and monitoring plasmon-enhanced reactions by optical nanoantennas coupled to photocatalytic beads. *Small* **2013**, *9*, 3301–3307.

[25] Nicoli, F.; Verschueren, D.; Klein, M.; Dekker, C.; Jonsson, M. P. DNA translocations through solid-state plasmonic nanopores. *Nano Lett.* **2014**, *14*, 6917–6925.

[26] Fromm, D. P.; Sundaramurthy, A.; Schuck, P. J.; Kino, G.; Moerner, W. E. Gap-dependent optical coupling of single "bowtie" nanoantennas resonant in the visible. *Nano Lett.* **2004**, *4*, 957–961.

[27] Liow, C.; Meng, F. B.; Chen, X. D.; Li, S. Z. Dependence of plasmonic properties on electron densities for various coupled Au nanostructures. *J. Phys. Chem. C* **2014**, *118*, 27531–27538.

[28] Novotny, L.; Bian, R. X.; Xie, X. S. Theory of nanometric optical tweezers. *Phys. Rev. Lett.* **1997**, *79*, 645–648.

[29] Gramotnev, D. K.; Bozhevolnyi, S. I. Nanofocusing of electromagnetic radiation. *Nat. Photonics* **2013**, *8*, 13–22.

[30] Halas, N. J.; Lal, S.; Link, S.; Chang, W. S.; Natelson, D.; Hafner, J. H.; Nordlander, P. A plethora of plasmonics from the laboratory for nanophotonics at Rice University. *Adv. Mater.* **2012**, *24*, 4842–4877, 4774.

[31] Schuck, P. J.; Fromm, D. P.; Sundaramurthy, A.; Kino, G. S.; Moerner, W. E. Improving the mismatch between light and nanoscale objects with gold bowtie nanoantennas. *Phys. Rev. Lett.* **2005**, *94*, 017402.

[32] Liaw, J.-W. Analysis of a bowtie nanoantenna for the enhancement of spontaneous emission. *IEEE J. Sel. Top. Quantum Electron.* **2008**, *14*, 1441–1447.

[33] Sundaramurthy, A.; Schuck, P. J.; Conley, N. R.; Fromm, D. P.; Kino, G. S.; Moerner, W. E. Toward nanometer-scale optical photolithography: Utilizing the near-field of bowtie optical nanoantennas. *Nano Lett.* **2006**, *6*, 355–360.

[34] Merlein, J.; Kahl, M.; Zuschlag, A.; Sell, A.; Halm, A.; Boneberg, J.; Leiderer, P.; Leitenstorfer, A.; Bratschitsch, R. Nanomechanical control of an optical antenna. *Nat. Photonics* **2008**, *2*, 230–233.

[35] Li, A. R.; Li, S. Z. Large-volume hot spots in gold spiky nanoparticle dimers for high-performance surface-enhanced spectroscopy. *Nanoscale* **2014**, *6*, 12921–12928.

[36] Zhang, Z.; Weber-Bargioni, A.; Wu, S. W.; Dhuey, S.; Cabrini, S.; Schuck, P. J. Manipulating nanoscale light fields with the asymmetric bowtie nano-colorsorter. *Nano Lett.* **2009**, *9*, 4505–4509.

[37] Dmitriev, A.; Hägglund, C.; Chen, S.; Fredriksson, H.; Pakizeh, T.; Käll, M.; Sutherland, D. S. Enhanced nanoplasmonic optical sensors with reduced substrate effect. *Nano Lett.* **2008**, *8*, 3893–3898.

[38] Shen, Y.; Zhou, J. H.; Liu, T. R.; Tao, Y. T.; Jiang, R. B.; Liu, M. X.; Xiao, G. H.; Zhu, J. H.; Zhou, Z. K.; Wang, X. H. et al. Plasmonic gold mushroom arrays with refractive index sensing figures of merit approaching the theoretical limit. *Nat. Commun.* **2013**, *4*, 2381.

[39] Siegfried, T.; Ekinci, Y.; Martin, O. J. F.; Sigg, H. Gap plasmons and near-field enhancement in closely packed sub-10 nm gap resonators. *Nano Lett.* **2013**, *13*, 5449–5453.

[40] Artar, A.; Yanik, A. A.; Altug, H. Fabry-pérot nanocavities in multilayered plasmonic crystals for enhanced biosensing. *Appl. Phys. Lett.* **2009**, *95*, 051105.

[41] Gates, B. D.; Xu, Q.; Stewart, M.; Ryan, D.; Willson, C. G.; Whitesides, G. M. New approaches to nanofabrication: Molding, printing, and other techniques. *Chem. Rev.* **2005**, *105*, 1171–1196.

[42] Zrimsek, A. B.; Henry, A.-I.; Van Duyne, R. P. Single molecule surface-enhanced Raman spectroscopy without nanogaps. *J. Phys. Chem. Lett.* **2013**, *4*, 3206–3210.

[43] Rybczynski, J.; Hilgendorff, M.; Giersig, M. Nanosphere lithography—fabrication of various periodic magnetic particle arrays using versatile nanosphere masks. In *Low-dimensional Systems: Theory, Preparation, and some Applications*; Liz-Marzán, L. M.; Giersig, M., Eds.; Springer: Netherlands, 2003; pp 163–172.

[44] Sawaguchi, T.; Mizutani, F.; Yoshimoto, S.; Taniguchi, I. Voltammetric and *in situ* STM studies on self-assembled monolayers of 4-mercaptopyridine, 2-mercaptopyridine and thiophenol on Au(111) electrodes. *Electrochim. Acta* **2000**, *45*, 2861–2867.

[45] Hu, J. W.; Zhao, B.; Xu, W. Q.; Li, B. F.; Fan, Y. G. Surface-enhanced Raman spectroscopy study on the structure changes of 4-mercaptopyridine adsorbed on silver substrates and silver colloids. *Spectrochim. Acta, Part A* **2002**, *58*, 2827–2834.

[46] Liu, N.; Giessen, H. Coupling effects in optical metamaterials. *Angew. Chem., Int. Ed.* **2010**, *49*, 9838–9852.

[47] Taubert, R.; Ameling, R.; Weiss, T.; Christ, A.; Giessen, H. From near-field to far-field coupling in the third dimension: Retarded interaction of particle plasmons. *Nano Lett.* **2011**, *11*, 4421–4424.

[48] Li, G. Z.; Shen, Y.; Xiao, G. H.; Jin, C. J. Double-layered metal grating for high-performance refractive index sensing. *Opt. Express* **2015**, *23*, 8995–9003.

[49] Liu, T. R.; Shen, Y.; Shin, W.; Zhu, Q. Z.; Fan, S. H.; Jin, C. J. Dislocated double-layer metal gratings: An efficient unidirectional coupler. *Nano Lett.* **2014**, *14*, 3848–3854.

[50] Lyvers, D. P.; Moon, J. M.; Kildishev, A. V.; Shalaev, V. M.; Wei, A. Gold nanorod arrays as plasmonic cavity resonators. *ACS Nano* **2008**, *2*, 2569–2576.

[51] Doherty, M. D.; Murphy, A.; Pollard, R. J.; Dawson, P. Surface-enhanced Raman scattering from metallic nano-structures: Bridging the gap between the near-field and far-field responses. *Phys. Rev. X* **2013**, *3*, 011001.

[52] Raut, H. K.; Ganesh, V. A.; Nair, A. S.; Ramakrishna, S. Anti-reflective coatings: A critical, in-depth review. *Energy Environ. Sci.* **2011**, *4*, 3779–3804.

[53] Im, H.; Bantz, K. C.; Lee, S. H.; Johnson, T. W.; Haynes, C. L.; Oh, S. H. Self-assembled plasmonic nanoring cavity arrays for SERS and LSPR biosensing. *Adv. Mater.* **2013**, *25*, 2678–2685.

[54] Xu, H. B.; Lu, N.; Qi, D. P.; Hao, J. Y.; Gao, L. G.; Zhang, B.; Chi, L. F. Biomimetic antireflective Si nanopillar arrays. *Small* **2008**, *4*, 1972–1975.

[55] Palik, E. D. *Handbook of Optical Constants of Solids*; Academic Press: Orlando, FL, 1985.